Design and Modeling of the Hybrid Portable Gamma Camera System

L.E. Smith, Z. He, D.K. Wehe, G.F. Knoll, S.J. Wilderman
Department of Nuclear Engineering and Radiological Sciences
University of Michigan
2355 Bonisteel Blvd., Ann Arbor, Michigan 48109-2104

Abstract

The combination of a mechanically-collimated camera with an electronically-collimated camera offers both the high efficiency and good angular resolution typical in a mechanically-collimated camera for lower energies and the uncoupling of spatial resolution and efficiency provided by an electronically-collimated camera at higher energies. The application is an industrial gamma-ray imaging system with good angular resolution and efficiency over a broad energy range: 50 keV to 3 MeV. The design and performance modeling of the Hybrid Portable Gamma Camera, currently being built, is described here. The optimization of the Anger-logic first detector module in terms of spatial and energy resolution is accomplished using a Monte Carlo optical photon modeling code and Cramer-Rao lower bound calculations. Approximately 6 mm spatial resolution and 7.5% FWHM (statistical contribution only) energy resolution for a 140 keV incident energy are expected for the 100x100x10 mm^3 NaI(Tl) first detector. Analytical calculations of angular resolution components and efficiency for the Hybrid Portable Gamma Camera are compared to Monte Carlo calculations of the same quantities. The expected angular resolution performance for on-axis point sources, a central scattering angle of 30° and a detector separation distance of 35 cm ranges from 3-5° FWHM over the sensitive energy range. Intrinsic efficiency results over the same energy range are also presented.

I. Introduction

Portable photon imaging devices with a broad energy range of sensitivity, adequate angular resolution and high efficiency are useful in applications such as environmental remediation and industrial surveys. The vast majority of past systems built for these applications have relied on mechanical collimation (MC) although a few have used electronic collimation (EC). To our knowledge, no portable devices have been built that exploit the benefits of both mechanical and electronic collimation in the same system. The Hybrid Portable Gamma Camera (HPGC) seeks to fill this niche by combining a hexagonal uniformly redundant array (HURA) coded aperture camera with a Compton scatter camera. This paper provides the system description and analysis of the HPGC with specific attention to the critical imaging parameters: energy resolution, spatial resolution and efficiency over a broad range of energies: 50 keV to 3 MeV.[1]

II. System Description

The two photon imaging modalities utilized in the HPGC are well established. Multiplexed imaging using a spatially coded mask has been used extensively in astrophysics [1] and Compton cameras have been well described by other investigators [2],[3],[4]. Combining the information from the MC and EC data sets to complement one another has recently been researched by Gormley [5]. However, using the same detection system for both methods has not been attempted and offers some unique challenges, particularly for the first detector design.

The desired imaging event for incident photons with energies less than 300 keV is a photoelectric absorption in the first detector after passing through one of the coded mask's open elements. For higher energy photons (above 600 keV), the coded mask will not be a significant attenuator and the ideal event is a Compton scatter in the first detector followed by photoelectric absorption in the second detector. At intermediate energies (300-600 keV), the MC and EC data sets will be combined in the image reconstruction phase. The use of a HURA mask design allows background subtraction through rotation of the mask (either 60° or 180°) which will reduce the deleterious effects of radiation incident from the sides of the system and scattering in the mask before interaction in the first detector. Figure 1 shows the HPGC system arrangement.

The first detector, which acts as both the coded aperture imaging detector and the scattering detector for the EC portion of the system must have the following characteristics.

1) Adequate spatial resolution (less than 7 mm FWHM) to minimize the effect of first detector event location on coded aperture reconstruction and backprojection cone axis reconstruction in the EC portion of the camera.

2) Adequate energy resolution (less than 7% at 662 keV) to minimize cone angle uncertainty from the relative energy depositions in the first and second detectors for the EC portion of the camera and also to provide spectral energy separation when viewing polyenergetic sources.

3) Relatively large area and stopping power (more than 80 cm^2, greater than 90% at 140 keV) so that a full cycle of the coded mask can be projected on the useable area and efficiency is maximized.

4) Reasonably portable: compact module with simple readout scheme.

* This work supported under DOE Grant DE-FG02-86NE37969

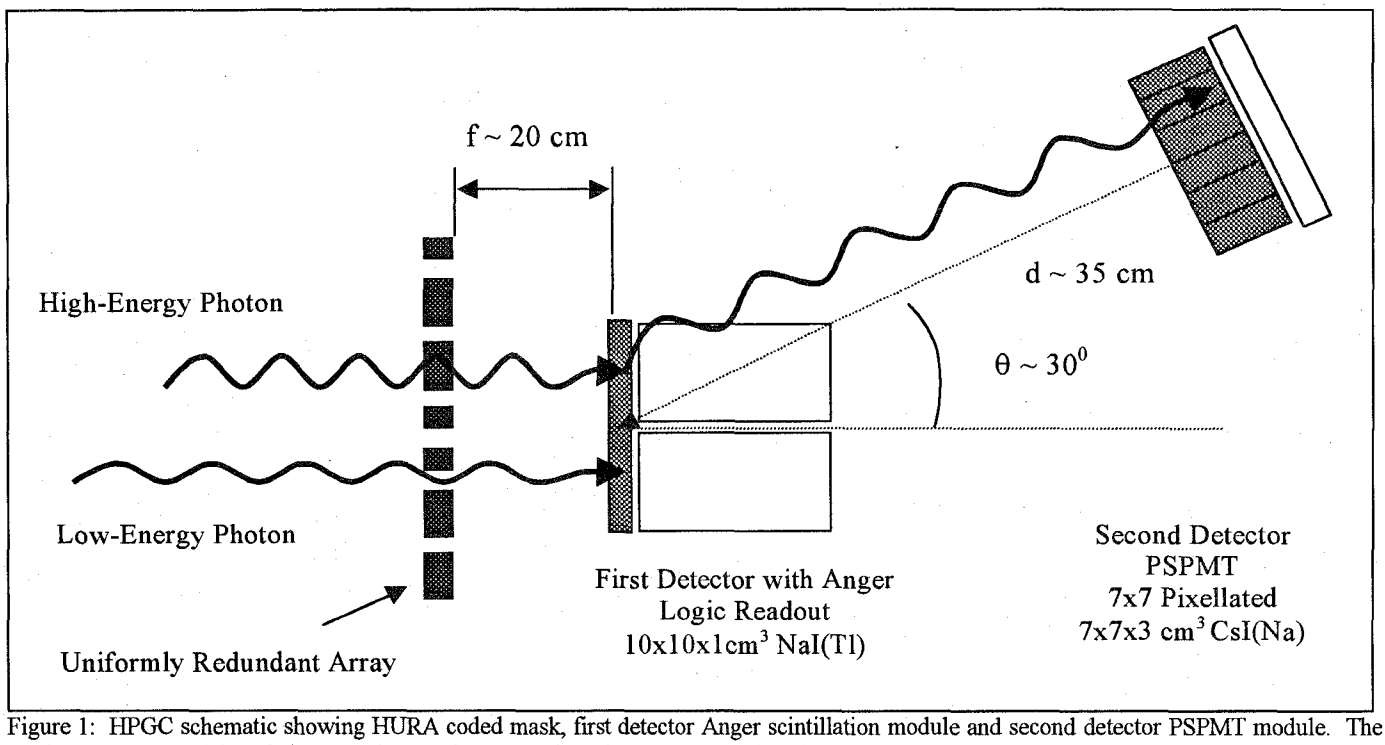

Figure 1: HPGC schematic showing HURA coded mask, first detector Anger scintillation module and second detector PSPMT module. The mask-to-detector spacing, f, the central scattering angle, θ, and the detector separation distance, d, are also shown for the proposed system.

The first two criteria favor the use of pixellated semiconductor materials such as germanium or CZT, but the need for large area, portable devices make them impractical The logical choice becomes a scintillation detector coupled to either a position sensitive photomultiplier tube (PSPMT) or an array of photomultiplier tubes (PMTs) in an Anger scheme. The Anger scheme can offer a larger detection area and nearly the same spatial and energy resolution as a PSPMT for relatively thick scintillator crystals at a much reduced cost [6]. Since energy resolution is at a premium, NaI(Tl) is the appropriate scintillator material and a first detector consisting of a 100x100x10 mm^3 crystal coupled to four 51 mm diameter PMTs has been constructed. The specific edge and surface treatments of the crystal are discussed in the next section describing the first detector design.

The second detector requirements are somewhat relaxed in terms of energy resolution, but spatial resolution is again an important factor in conical axis reconstruction in the EC portion of the camera. Stopping power is of paramount importance to maximize the peak-to-total ratio in the second detector and increase system efficiency. Although CsI(Na) has lower light output than NaI(Tl), the higher Z value makes it preferable for a second detector material. A 7x7 pixellated CsI(Na) array with 9x9x30 mm^3 pixels is coupled to a Hamamatsu R3941 PSPMT. The use of a PSPMT with a pixellated array is largely due to the availability of the unit to our group and is somewhat superfluous since the excellent intrinsic resolution of the PSPMT is not well utilized when coupled to a pixellated array. However, the readout scheme is straightforward with the PSPMT; a fortunate benefit of the high intrinsic resolution is scatter rejection in the second detector based on the light centroid locations from the individual pixels of the crystal. An event location that differs greatly from the well-defined light centroid positions of the individual pixels is presumed to be the result of a multiple scatter involving two or more pixels.

III. First Detector Design and Modeling

In order to achieve a crystal design that optimizes both spatial resolution and energy resolution for a given crystal size and readout scheme, modeling of the light produced by the gamma interaction in the scintillation crystal was done. DETECT, a Monte Carlo code for modeling the optical properties of scintillators [7], was used to generate the light spread function and the PMT responses to that light spread function. Over 40 different combinations of surface treatments and light guide thicknesses were modeled and compared on the basis of the best spatial and energy resolution that each design would provide. Quantifying the energy resolution is straightforward and is simply related to the total number of photoelectrons created at the photocathodes of the PMTs. Quantifying the spatial resolution is more involved and is best done using the Cramer-Rao lower bound (CRLB) on estimator variance.

The CRLB is a valuable tool for determining the intrinsic quality of the measurements and can be used to determine the optimum design parameters for the crystal based only on the PMT mean response. The use of the CRLB as a system performance estimator is described in detail by Clinthorne [8],[9] and is only summarized here.

There are two essential components for the bound calculations: a finite parameterization of the source, ϕ, and a statistical model, represented by the conditional probability density $f(\mathbf{y} \mid \phi)$, which relates these parameters to a vector of N measurements, $\mathbf{y} = [y_1,\ldots,y_N]^T$. The calculation of the

limiting spatial resolution for different crystal designs was performed in only one dimension for simplicity. In this case, the mean measurements as a function of position are given by $S_i(x)$, the average signal (number of photoelectrons) produced in the ith PMT as a function of source position, x. These values represent the parameterization of the source. Since the production and detection of scintillation photons are assumed to be Poisson processes, the probability density function (PDF) relating a set of PMT measurements M_i for an event is given by

$$p(\underline{M}|x) = \prod_{i=1}^{4} \frac{S_i(x)^{M_i} e^{-s_i(x)}}{M_i!} \quad (1)$$

σ_{lb}^2, the lower bound on spatial variance, is related to the PDF in the following way:

$$\sigma_{lb}^2 = \frac{1}{-E\left[\frac{\partial^2 \ln p(\underline{M}|x)}{\partial x^2}\right]} \quad (2)$$

The limiting variance on position estimation takes on the simple form:

$$\sigma_{lb}^2 = \left[\sum_{i=1}^{4} \frac{(\partial S_i(x)/\partial x)^2}{S_i(x)}\right]^{-1} \quad (3)$$

This variance represents the lowest achievable spatial resolution as a function of position for the given probability density function and source parameterization values, $S_i(x)$. It is clear from this equation that the shape of $S_i(x)$, the PMT mean response curves, is the most important factor in determining the position estimator variance and ultimately the spatial resolution of the detector system.

A photon source was scanned across the face ($-50<x<0$ mm and $y=0$ mm, where $x=y=0$ is the center of the crystal) of a 100x100x10 mm^3 NaI(Tl) crystal coupled to a glass 100x100x15 mm^3 light guide which is in turn coupled to the four PMTs. The mean response functions, $S_i(x)$, were determined. Using the above CRLB analysis, the limiting spatial variance for all new designs was compared to two extreme designs: one optimized in terms of spatial resolution and the other in terms of energy resolution. The first design is the one most commonly employed in systems of this type and uses blackened, absorbing edges with a diffusely reflecting top face. The second design has diffusely reflective surface treatments on the crystal edges and top face (incident radiation side).

Although several crystal designs showed promising performance, the most practical to implement is shown in Figure 2 and consists of a 5mm strip of gray absorbing paint on the top face (incident radiation side) perimeter and a 10 mm polished, specularly reflecting strip inside of the gray strip.

The mean response functions for the two comparison cases and the new design are shown in Figure 3. These results are

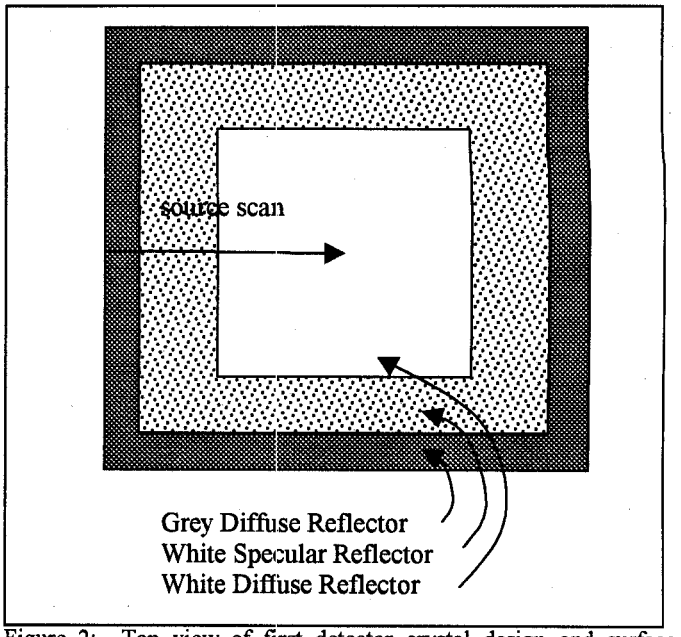

Figure 2: Top view of first detector crystal design and surface treatments

based on the average signal from 80 photoelectric interactions of a 140 keV photon at each x position. The depth of interaction in the crystal is uniformly spread over the 10 mm thickness and a quantum efficiency of 0.22 is assumed for the photocathodes. Because the source is scanned across the center of the crystal, two of the PMT signals will on average, be equal. To decrease the statistical fluctuations in the $S_i(x)$ values, these two PMT signals were averaged before plotting, resulting in only 2 PMT signals for display.

Of particular note in Figure 3 is the difference in the magnitudes of the mean response functions and the shape of these response functions near the edge of the crystal ($x=-50$mm). All three designs perform similarly near the center of the crystal since the direct light contribution dominates the light spread function. Closer to the edges, the diffuse light becomes significant, skewing the light spread function. Tailoring this contribution is the key to extending the useable area of the detector.

In the first design, the blackened edges absorb much of the diffuse light, resulting in fewer collected photons and inducing a sharp decrease in the PMT signals near the edge. The signals at the edge, however, are unique at each position and good spatial resolution is achieved over nearly all of the detector (Figure 4). In the second design, the reflecting edges reflect much of the diffuse light, resulting in large tails in the light spread function and a flattening effect on the mean response functions. In addition, a double valued region extends from $-50<x<-35$ since all of the produced light is conserved. The ambiguity in the signals in this region make it useless for event location and only about 50% of the detector area is useable in the fully reflecting design.

The new design provides enough absorption near the edges that a drop occurs in the near-side PMT signal, but has little effect on the far-side PMT signal. No double-valued regions exist and most of the original scintillation light is collected at

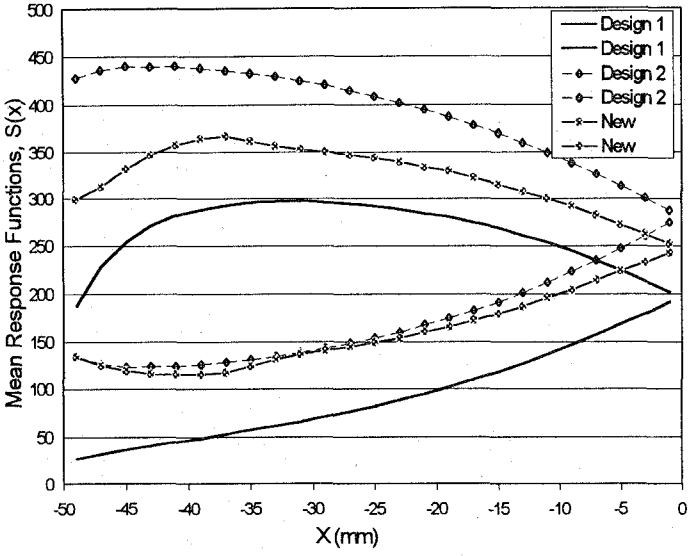

Figure 3: Mean response functions, $S_i(x)$ for black edges (design 1), reflecting edges (design 2) and new design.

the photocathode. By placing the absorbing strip on the top of the crystal instead of the side, only interactions near the edge will lose a significant amount of light due to absorption at the crystal surfaces. The mean response function is effectively tailored near the edges to extend the useful detection area, but good energy resolution is maintained over the entire face of the crystal.

The percentage FWHM energy resolution due to photon statistics alone and the CRLB for spatial resolution for the two comparison cases and the new design are calculated based on the mean response functions in Figure 3 and are shown in Figure 4.

IV. HPGC System Performance Modeling

A. System Energy Resolution

The energy resolution for the MC portion of the camera is solely defined by the first detector NaI(Tl) crystal. Assuming PMT noise is negligible and scintillation statistics are the dominant factor in the energy resolution, the relationship should be $\sigma_{MC} = (k_1 E)^{1/2}$ keV where k_1 is a first detector constant of approximately 0.6 based on the expected resolution of 7% at 662 keV for the NaI(Tl) crystal. The summed energy resolution for the EC data will be dependent on the quadrature sum of the resolutions of the first and second detectors: $\sigma_{EC}^2 = (\sigma_{MC}^2 + \sigma_2^2)^{1/2}$ where σ_2 is defined as above with k_2=2.0 for the CsI(Na) crystal (based on measured resolution value of 13% at 662 keV).

B. System Angular Resolution Modeling

Only on-axis point sources at least 30 cm from the first detector are considered in the following analysis. The angular resolution of a far-field HURA imaging system (magnification value of unity) is defined by the mask-to-detector spacing, f, the mask element size, c, and the intrinsic spatial resolution of the detection area, e. The mask element size is generally set

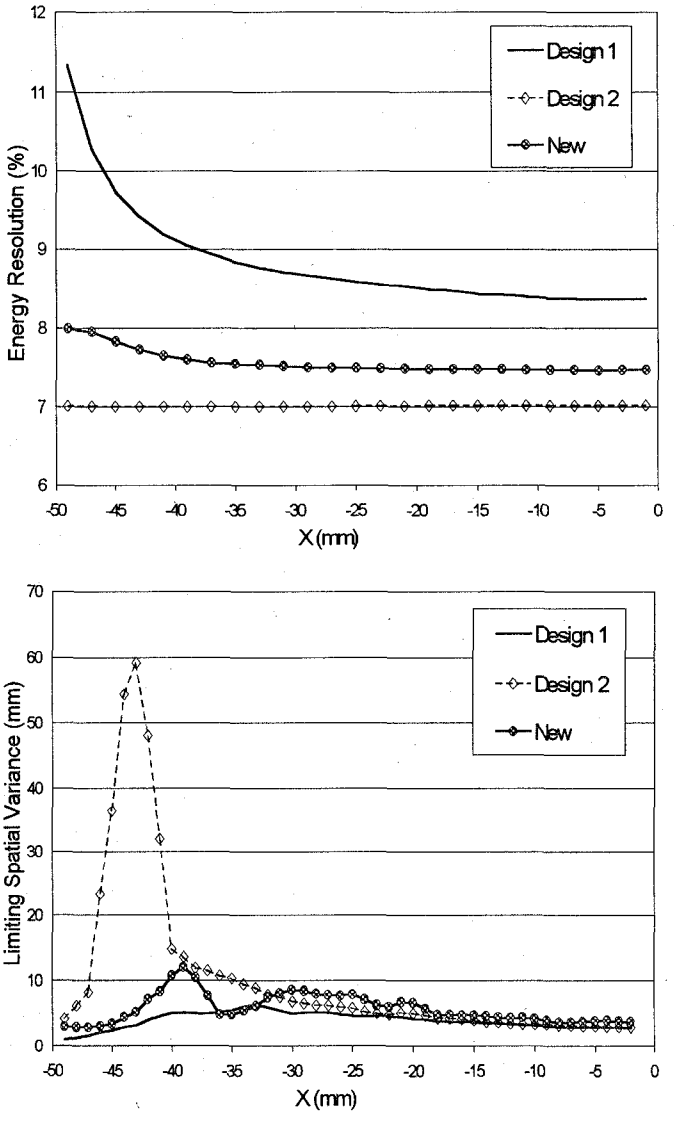

Figure 4: Statistical contribution to energy resolution (top) and limiting spatial variance (bottom) for the two comparison designs and the new design.

equal to twice the value of e. The relationship between the angular resolution, $\Delta\alpha$, and these values is $\Delta\alpha = c/f = 2e/f$ [1]. The MC module of our system will have an angular uncertainty of approximately 4°. Using a conservative first detector average intrinsic spatial resolution of 7mm based on the CRLB spatial variance calculations for the new crystal design, a mask-to-detector spacing of approximately 20 cm is required (Figure 1).

The angular resolution calculation for electronic collimation is more involved. The backprojection cone is defined by both a cone axis and a cone angle. The uncertainty in the cone axis is a function of the uncertainty in the interaction site locations of each detector. The cone angle uncertainty is determined by the uncertainty in the relative energy depositions in the two detectors. The total angular resolution is commonly separated into two components: the energy uncertainty term $\Delta\theta_e$ and the geometric uncertainty term $\Delta\theta_g$. The two terms add in

tangential quadrature to yield the total angular uncertainty of *an event [3]*:

$$\tan^2(\Delta\theta_{tot}) = \tan^2(\Delta\theta_g) + \tan^2(\Delta\theta_e) \quad (4)$$

The calculation of these components is complicated by the fact that there is a range of possible scattering angles that can occur for a given central scattering angle, θ, in the HPGC geometry. For instance, if the central scattering angle is 30° and the detector separation distance is 35 cm, scatters can occur through a range of 17-42° for a far-field, on-axis point source. In the analytical modeling of these components, numerical integration and averaging over the angular range of interest were used to calculate the FWHM of the effects contributing to the overall spatial resolution: lateral resolution of first detector, thickness of first detector, lateral resolution and thickness of second detector, and energy resolution of the first detector. A spreadsheet program was used to vary the relevant system parameters (first or second detector size, energy resolution of first detector, central scattering angle, and detector separation distance) and calculate the expected angular resolution components.

To benchmark the analytical expressions used in the spreadsheet calculations, the data were compared to a Monte Carlo calculation of the point spread function for Compton scatter cameras. SKEPTIC, a vectorized algorithm for Monte Carlo simulation of photon transport, generates detailed records of the exact energy loss and positions of interactions in the detection system for each particle emitted from the source [10]. A list mode file of all coincident interactions is used as input to the PSF companion code. This PSF code uses the known performance characteristics of the two detectors (energy resolution, spatial resolution, lower level descriminator, upper level descriminator) and samples from a Gaussian distribution defined by these parameters for each energy deposition and interaction position. The net result is a blurring of each of the exact energy and position values and a construction of the backprojection cone for that particular event based on these blurred values. Calculating the closest approach of the cone to the known source point using the simulated measurement data for each valid coincident event, the various components of the total angular resolution and the overall point spread function can be determined. Figure 5 compares the analytical values and the Monte Carlo values of the angular resolution components for a single test case.

Plotting the resolution components over a range of system parameter values provides a valuable system analysis tool. Figure 6 shows the system angular resolution as a function of incident energy for both the analytical model and the Monte Carlo simulations.

There was good agreement between the analytical and Monte Carlo values over a wide range of incident energies (412 keV-1173 keV), central scattering angles (20°-60°) and detector separations distances (25-55 cm), verifying the use of the analytical modeling to predict trends in system angular resolution performance and the viability of the HPGC design.

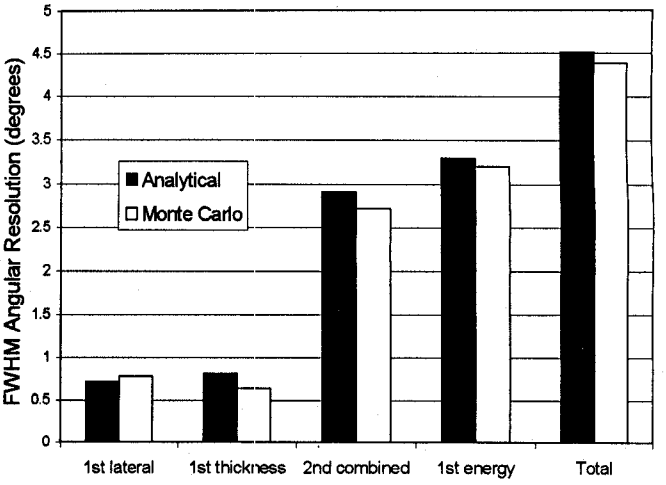

Figure 5: Comparison of analytical and Monte Carlo calculations of angular resolution components for system parameters: θ = 30°, d = 35 cm, E = 662 keV.

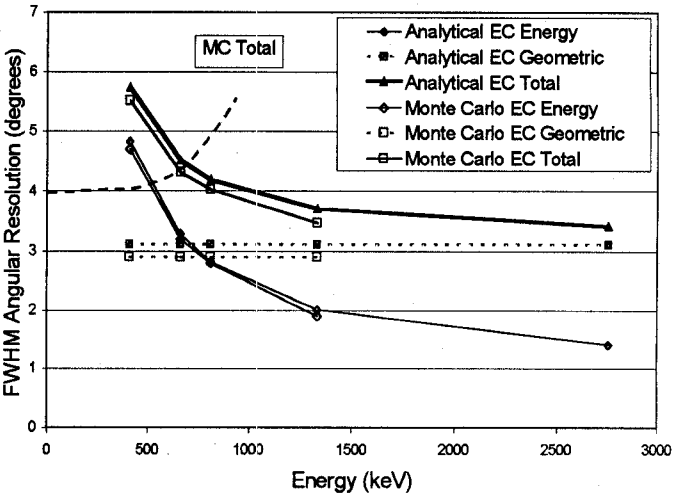

Figure 6: System angular resolution as function of incident photon energy for θ = 30° and d = 35cm.

C. *Efficiency Modeling*

Only the intrinsic efficiency of the HPGC is considered here since it is a far-field imager. The intrinsic peak efficiency of the MC module will depend on the probability of interaction in the NaI(Tl) first detector, the peak-to-total ratio at the incident energy and the open fraction of the HURA mask (~0.5). The Monte Carlo calculations of the MC intrinsic efficiency are shown below in Figure 7 [11].

The analytical efficiency modeling for the Compton events employed numerical integration techniques and empirically fit cross-sections [12] along with Klein-Nishina differential scattering cross-section weighting to calculate the intrinsic efficiency of the EC camera. The general formula for the intrinsic Compton efficiency ε_{ic} is defined as:

$$\varepsilon_{ic} = P_c \varepsilon_{g2} \varepsilon_{ip2} \quad (5)$$

This EC intrinsic efficiency is the probability that a gamma ray incident on the first detector will result in a useful imaging event—it does not depend on source position. P_c is the probability that a gamma ray incident on the first detector will undergo a Compton scatter and escape into the angular range subtended by the second detector. Once a scattered gamma ray escapes the first detector in the proper angular range, it must strike the second detector. The probability of this occurring is simply the fraction of the total scattering area that the second detector subtends, ε_{g2}. The final factor in the intrinsic Compton efficiency equation is the intrinsic peak efficiency of the second detector, ε_{ip2}.

Again, the analytical calculations were compared with the Monte Carlo results for a number of different configurations. The modeling is somewhat conservative in that a first detector useful area of only 70x70 mm^2 is assumed, rather than the 100x100 mm^2 actual area since the useful area will depend on the effectiveness of the event location algorithm used for the first detector. The analytical and Monte Carlo values agreed very well over a broad range of energies, central scattering angles, and detector separation distances, indicating that the analytical model can be used to estimate system intrinsic efficiency performance. A comparison of the Monte Carlo and analytical calculations of intrinsic efficiency for a few system configurations is shown in Figure 7. The HPGC intrinsic efficiency variation as a function of energy is plotted in Figure 8 for $\theta = 30°$ and d = 35 cm.

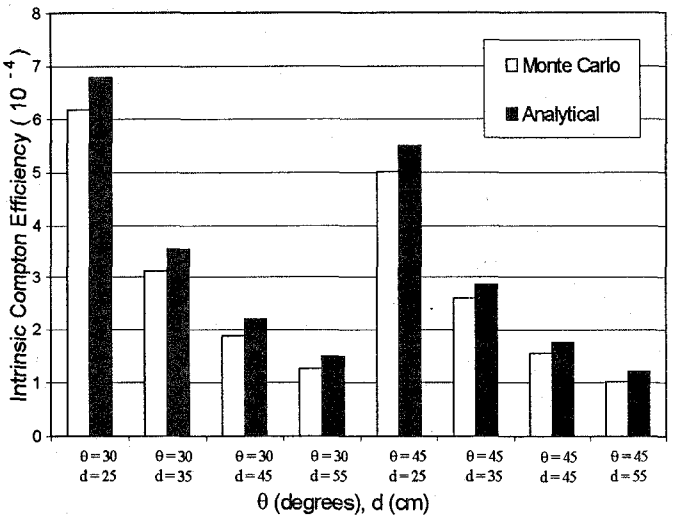

Figure 7: Comparison of analytical and Monte Carlo calculations of intrinsic electronic collimation efficiency variation for E=662 keV.

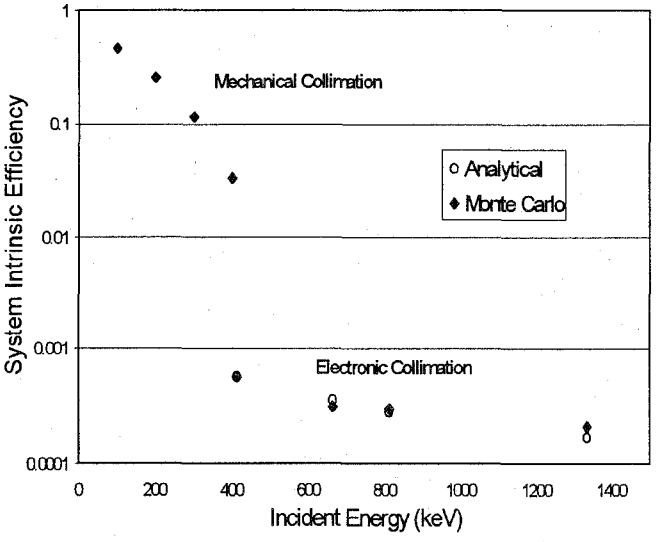

Figure 8: HPGC intrinsic efficiency variation with incident energy for $\theta = 30°$ and d = 35cm.

V. Conclusions

A hybrid imaging system combining coded aperture and Compton scatter imaging has been designed and modeled. The new first detector crystal design provides improved energy resolution and spatial resolution comparable to that achievable in the blackened edge design commonly used for thick scintillation crystals. Analytical modeling of the system in terms of angular resolution and intrinsic detection efficiency was performed and verified using Monte Carlo calculations of the same quantities. The most appropriate system parameters to strike a balance between intrinsic efficiency and angular resolution were determined to be a central scattering angle of 30°, a detector separation distance of 35 cm and a mask-to-detector spacing of 20 cm. The system achieves an intrinsic efficiency ranging from ~0.50 to ~$1x10^{-4}$ and an angular resolution of 3-5° over the sensitive energy range of the system: 50 keV to 3 MeV.

VI. References

[1] E.E. Fenimore and T.M. Cannon, "Coded aperture imaging with uniformly redundant arrays," *Applied Optics*, vol. 17, no. 3, pp. 337-346, February 1978.

[2] J.B. Martin, et al., "A Ring Compton Camera for Imaging Medium Energy Gamma Rays," *IEEE Transactions on Nuclear Science*, vol. 40, no.4, pp. 972-978, August 1993.

[3] M. Singh, "An electronically collimated gamma camera for single photon emission computed tomography. Part I: Theoretical Consideration and Design Criteria," *Medical Physics*, vol. 10, no.4, pp. 421-427, July-August 1983.

[4] J. B. Martin, et al., "Imaging Multi-Energy Gamma-Ray Fields with a Compton Scatter Camera," *IEEE Transactions on Nuclear Science*, vol. 41, pp. 1019-1025, August 1994.

[5] J. Gormley, *Experimental Comparison of Mechanical and Electronic Gamma-Ray Collimation*, Ph.D. dissertation, The University of Michigan, Ann Arbor, MI, 1994.

[6] T.D. Milster, et al., "A Full-Field Modular Gamma Camera," *The Journal of Nuclear Medicine*, vol. 31, no. 4, pp. 632-639, April 1990.

[7] *DETECT: A Program for Modeling Optical Properties of Scintillators*, G.F. Knoll and T.F. Knoll, User Manual for DETECT97, A. Levin, et al., November 20, 1996.

[8] N.H. Clinthorne, et al., "Determining Detector Requirements for Medical Imaging Applications," Unpublished.

[9] N.H. Clinthorne, et al., "A Hybrid Maximum Likelihood Position Computer for Scintillation Cameras," *IEEE Transactions on Nuclear Science*, vol. 34, no. 1, February 1997.

[10] S.J. Wilderman, *Vectorized algorithms for the Monte Carlo simulation of kilovolt electron and photon transport*, Ph.D. dissertation, The University of Michigan, Ann Arbor, MI, 1990.

[11] *GEANT Detector Description and Simulation Tool*, Version 3.16, Applications Software Group, CERN, Geneva, Switzerland, March 1994.

[12] J.H. Hubbel, *Photon Cross Sections, Attenuation Coefficients, and Energy Absorption Coefficients for 10 keV to 100 GeV*, U.S. Department of Commerce, National Bureau of Standards, August 1969.